Tin Modified Carbon Nanofibers as an Effective Catalytic Electrode for Bromine Redox Reactions in Static Zinc-bromine Batteries

Masud Rana,[a] Craig T. Stoppiello,[b] Qiu He,[d] Xiyue Peng,[a] Norah Alghamdi,[a, c, e] Yongxin Huang,[a] Ian R. Gentle,[c] and Bin Luo*[a]

Zinc-bromine batteries (ZBBs) have emerged as a compelling solution for large-scale energy storage, yet they confront significant technical challenges impeding widespread commercialization. The electrochemical processes within ZBBs rely on a stoichiometric mechanism, where the bromine reaction at the cathode drives the zinc plating reaction on the anode. However, the sluggish electrochemical kinetics of Br_2/Br^- redox reactions lead to substantial electrochemical polarization, resulting in interruptions in zinc plating and significant voltage losses in ZBBs. This study introduces a new solution to address these challenges by leveraging carbon nanofiber decorated with tin nanoparticles as an efficient catalyst. The catalyst serves to enhance the Br_2/Br^- redox reaction, effectively reducing voltage losses in ZBBs. When implemented in static ZBB configurations, the Sn/CNF catalysts demonstrate exceptional long-term stability, achieving an impressive 3000 cycles with minimal voltage loss. In contrast, ZBBs utilizing SnO_2 based catalysts experience a substantially higher voltage loss of 736 mV, along with limited and unstable cycling performance. These findings signify a promising approach for the development of catalytic electrodes, paving the way for high-performance ZBBs with improved efficiency and cycling durability.

Introduction

Electrical power generation from renewable and sustainable energy sources has become a high priority due to the worldwide energy crisis. Approximately 68% of today's electrical energy is supplied from fossil fuels: coal (42%), natural gas (21%), oil (5%), with nuclear (14%), hydro (15%), and the remaining 3% from renewable energy technologies.[1] Unfortunately, renewable energy sources are inherently intermittent and naturally unpredictable resources, including sunlight, ocean tides, and wind. Hence, the power grid systems across the globe cannot rely solely on these sustainable sources as they seriously destabilize the electrical grid.[2] Environmental pollution some existing energy sources is another concern in the upcoming decades. Every kWh of electricity generated by burning coal coproduces an average 1000 g lifecycle CO_2 emission, a greenhouse gas that is widely considered as the primary contributor to global warming.[3] In the United States alone, coal power plants emit 1.5 billion tons of CO_2 per year, and emissions from developing countries continue to accelerate.[4] Fossil fuels are the main sources of CO_2 emissions which accounted for 87% of the global energy supply in 2012.[5] To reduce greenhouse gas emissions, most countries are adopting emission regulations and developing reliable low emission renewable energy storage systems. The European Union has lowered the CO_2 emissions by 17% from 1990 to 2012 and plans to reduce by a further 20% by 2020. Recently, Australia has adopted a decarbonization plan to reduce over half of Australia's total CO_2 emissions based on renewable energy generation supported by energy storage.[6] In the United States, nearly 120 million homes consumes energy from the renewable energy sources to decarbonize the residential sector.[7] To fulfill these targets, battery-based energy storage systems, along with rapid charge/discharge responses, are inevitable for desirable load levelling in renewable power generation.[8] Reliable and sustainable green energy supply and storage systems are highly desired to solve these existing problems.

Among the alternative energy storage systems available or in development for grid-scale storage, zinc-bromine flow batteries (ZBFBs) are regarded as a practically viable alternative for large-scale stationary energy storage applications due to

[a] Dr. M. Rana, Dr. X. Peng, N. Alghamdi, Y. Huang, Dr. B. Luo
Australian Institute for Bioengineering and Nanotechnology (AIBN), The University of Queensland, 4072 Brisbane, QLD, Australia
E-mail: b.luo1@uq.edu.au

[b] Dr. C. T. Stoppiello
Centre for Microscopy and Microanalysis, The University of Queensland, 4072 Brisbane, QLD, Australia

[c] N. Alghamdi, Prof. I. R. Gentle
School of Chemistry and Molecular Biosciences, Faculty of Science, The University of Queensland, 4072 St Lucia, QLD, Australia
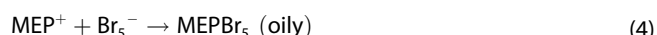
[d] Dr. Q. He
State School Key Laboratory of Silicate Materials for Architectures, International School of Materials Science and Engineering, Wuhan University of Technology, 430070 Wuhan, Hubei, China

[e] N. Alghamdi
Department of Chemistry, Faculty of Science, Imam Mohammad Ibn Saud Islamic University (IMSIU), 11564 Riyadh, Saudi Arabia

their appealing features such as high-safety recyclability, eco-friendliness, high cell voltage and high energy density.[9] ZBFBs exhibit a low levelized cost of energy stored (LCOES) ($/kWh/cycle/%) of 0.017 in comparison with vanadium redox flow batteries (0.065), and lithium ion batteries (0.58).[10] However, ZBFBs still face technical issues which require further mitigations strategies for large-scale electric grid applications. The high polarization of the polybromide complex, as well as the sluggish reaction kinetics not only increase voltage loss but also affect their capacity. During charging, the Br_2 reacts with the Methyl Ethyl Pyrrolidinium Bromide (MEP) complex[11] and produces polybromide species such as Br_3^-, Br_5^- and Br_7^- as shown by the following reactions 1–6.

$$Br_2 + Br- \rightarrow Br_3^- \tag{1}$$

$$MEP^+ + Br_3^- \rightarrow MEPBr_3 \ (aq) \tag{2}$$

$$2Br_2 + Br- \rightarrow Br_5^- \tag{3}$$

$$MEP^+ + Br_5^- \rightarrow MEPBr_5 \ (oily) \tag{4}$$

$$3Br_2 + Br- \rightarrow Br_7^- \tag{5}$$

$$MEP^+ + Br_7^- \rightarrow MEPBr_7 \ (oily) \tag{6}$$

During discharge, the reverse conversion of these polybromide complexes into bromine requires the presence of a catalyst. Various attempts have been adopted to catalyse the Br_2/Br redox reactions. For example, titanium nitride (TiN) nanorods and N-doped graphene nanoplatelets were reported as effective catalysts for Br_2/Br^- redox reactions in ZBBs.[12–14] Cage-like porous carbon (CPC) with superior activity on Br_2/Br^- redox reaction and entrapping capability of Br_2 complex to further reduce crossover was also proposed and investigated as a highly active catalyst.[15] Recently, Zeng et al. reported a tin-bromine redox flow battery with a Sn reverse-electrodeposition process on the negative side, providing a new way for the application of tin based functional materials in redox flow batteries.[16]

New electrode designs that can facilitate faster conversion and storage of bromine species to achieve high performance ZBBs are highly desirable. Tin has also been proposed as an excellent metal catalyst which is relatively resistant to corrosion and can increase the wettability of the electrode.[17] In this research, we report tin-modified carbon nanofibers (Sn/CNF) as an efficient electrocatalyst to accelerate the electrochemical kinetics of Br_2/Br^-. The tin nanoparticle-decorated carbon nanofibers act as a catalyst to promote fast electron transport to the polybromide complex and accelerate the electrochemical conversion. Hence, our proposed static ZBBs show superior electrochemical performance and lower voltage loss compared to the bare electrodes, with a high coulombic efficiency of 89%. Owing to the highly reversible Br_2/Br^- reaction, the battery shows an ultra-stable cycling life of over 3,000 cycles with minimum self-discharge rate. Our static battery configuration offers a cost-effective and easy fabrication path for spreading the static ZBBs to practical applications.

Results and Discussion

Materials synthesis and characterizations

The synthesis process of the Sn/CNF is described in detail in the experimental section and the process is schematically shown in the Figure 1. Briefly, $SnCl_2 \cdot 2H_2O$ was used as a tin precursor and SnO_2/CNF was produced through the hydrothermal technique.[18] Later, SnO_2/CNF was further treated at 500 °C in the presence of argon to obtain the Sn/CNF. The physical appearance, the physical structure of the SnO_2/CNF and Sn/CNF was first investigated by scanning electron microscopy.

Figure 2a–f show the SEM images of the pristine CNF, SnO_2 and Sn decorated CNF samples, respectively. These images visually confirm the successful growth of SnO_2 coating on the CNF after the in-situ growth process (Figure 2b). The surface treatment of CNF in HNO_3 generates numerous functional groups, such as −COOH and −OH, serving as nucleation sites for the growth of SnO_2 nanoparticles on CNF. In the solution of $SnCl_2$ and HNO_3, Sn^{2+} ions can be easily converted to Sn^{4+} via chemical oxidation, reacting with the aforementioned func-
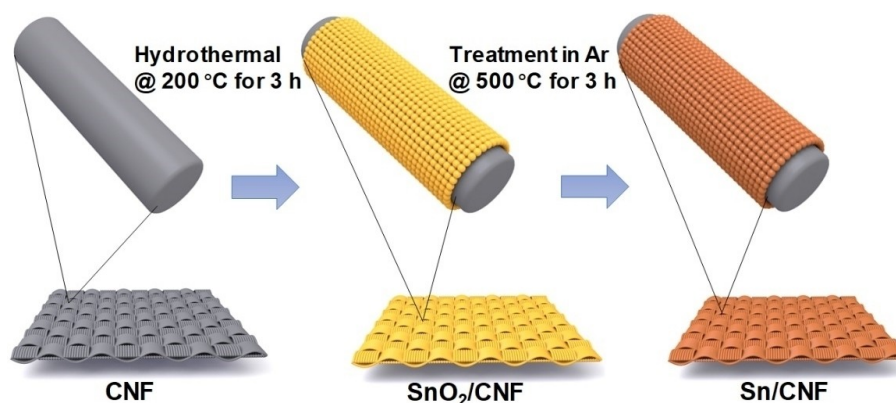

Figure 1. Schematic illustration of the SnO_2 and Sn decorated CNF synthesisation process.

Batteries & Supercaps

Research Article
doi.org/10.1002/batt.202300474

Chemistry Europe
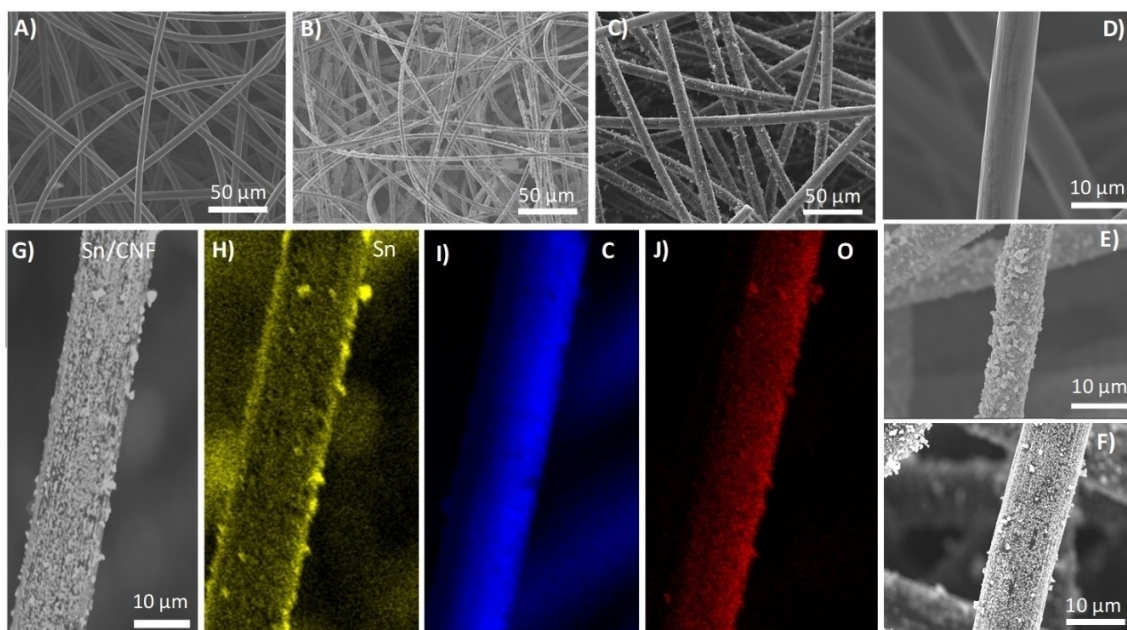European Chemical
Societies Publishing

Figure 2. (a) SEM images of pristine CNF (b) SnO₂ decorated CNF (SnO₂/CNF). (c) Sn decorated CNF (Sn/CNF) followed by their high magnification images shown in (d), (e) and (f), respectively. (g) Back scattered images of Sn/CNF. (h) EDS image of Sn/CNF indicates Sn coating on the surface. (i) Carbon and (j) Oxygen.

tional groups ($-COOH$ and $-OH$), eventually forming the SnO_2 coatingä.[19] Moreover, subjecting SnO_2/CNF to thermal treatment at 500 °C triggers the reduction of SnO_2 into metallic Sn while eliminating oxygen functional groups. This process notably transforms the $Sn-O-C$ bonds into $Sn-C-Sn$ bonds within Sn/CNF.[18,20,21]

The high-resolution images of pristine CNF, SnO_2 and Sn grown on CNF are separately displayed in Figure 2d–e. Notably, after the washing process, the 10 mm diameter cathode electrode coated with SnO_2/CNF exhibits a weight of 49 mg, while the Sn/CNF electrode shows 24 mg. The physical appearance indicates that the SnO_2 growth on the CNF is initially bulk. However, after the high temperature treatment the thickness has been significantly reduced in Sn/CNF, aligning with the observed weight loss. Elemental tracing via EDS analysis (Figure 2g–j) confirms the successful growth of Sn on the CNF surface, where Sn, carbon and oxygen are represented by yellow, blue and red colours, respectively, in the EDS images. Additionally, EDS scans of SnO_2/CNF and Sn/CNF suggest an increased carbon peak in Sn/CNF post thermal treatment (Figure S1).

The crystalline structure of the samples was investigated by X-ray diffraction (XRD). As shown in Figure 3a, two broad peaks at 26.2° and 43.8° in the XRD pattern signify pristine CNF, corresponding to the (002) and (100) crystalline planes of carbon, respectively. After the hydrothermal treatment, successful growth of SnO_2 on the CNF surface occured. The SnO_2/CNF (PDF 01-086-8925-SnO₂) exhibits peaks at 33.80°, 54.70° and 78.64°, denoting (101), (220) and (321) planes with lattice distances of 0.26 nm, 0.16 nm and 0.12 nm, respectively (Figure 3c). Following treatment in an argon atmosphere at 500 °C, the SnO_2/CNF transformed into Sn/CNF. After the high temper-

ature treatment, the Sn/CNF pattern shows intense carbon peak corresponding to the (002) and (100) crystalline planes of carbon. The Sn/CNF (PDF 03-065-0296-Sn) shows peaks at two theta of 31.38°, 32.78°, 44.94°, 46°, 56.68°, 64.02°, 66.14°, 74.14°, and 74.96°, indicating planes of (002), (200), (101), (220), (211), (112), (400), (321), (420), with (200), (101), (211) corresponding to the lattice distances of 0.29 nm, 0.27 nm and 0.20 nm, respectively (Figure 3d). A very thin layer of amorphous carbon coating on the tin particle is evident in the high-resolution image (Figure 3d). The crystalline structure of tin was further explored by high resolution STEM of dark field (DF), bright field (BF) and secondary electron imaging (SE). The presence of tin is demonstrated in the BF image as dark elements, and in the BF image as lighter elements, strongly supporting the high-resolution STEM analysis (Figure S3).

X-ray photoelectron spectroscopy (XPS) analysis was carried out to trace the elemental surface composition and understand how the chemical environments differ between the samples (Figure 4). The necessary peaks are levelled properly in Figure 4a. There are few unlevelled peaks in the Figure 4 a which is denoting to the Cl 2p3/2, Sn 4 s and Sn 4p. The atomic compositions of SnO_2/CNF and Sn/CNF are listed in Table S1 (Supporting information). SnO_2/CNF showed a high oxygen content of 39.5%, along with significant amounts of carbon (29.8%), chlorine (5.9%), and tin (24.9%) in the SnO_2/CNF. In contrast, Sn/CNF exhibited a much lower oxygen content of 4.0% and tin content of 1.13%, but a very high carbon content of 94.8% indicating again that the Sn/CNF is physically transformed and maintains maximum intensity of carbon with minor concentration of tin. This is also strongly supported by the high-resolution TEM images of tin particles surrounded by the amorphous carbon shown in Figure 3d. The significant decrease
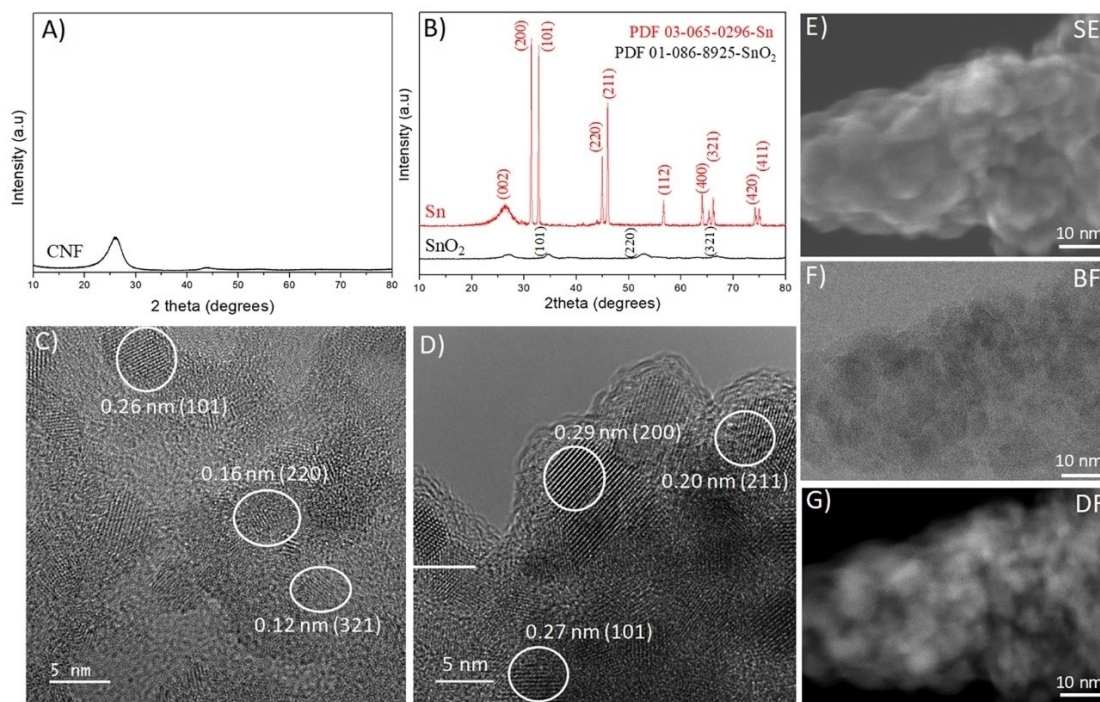
Figure 3. (a) XRD of pristine CNF, (b) XRD of SnO$_2$@CNF and Sn@CNF. (c) HRTEM image of SnO$_2$@CNF. (d) HRTEM image of Sn@CNF. (e–g) STEM image of Sn@CNF indicates secondary image (SE), bright field image (BF) and dark field image (DF).
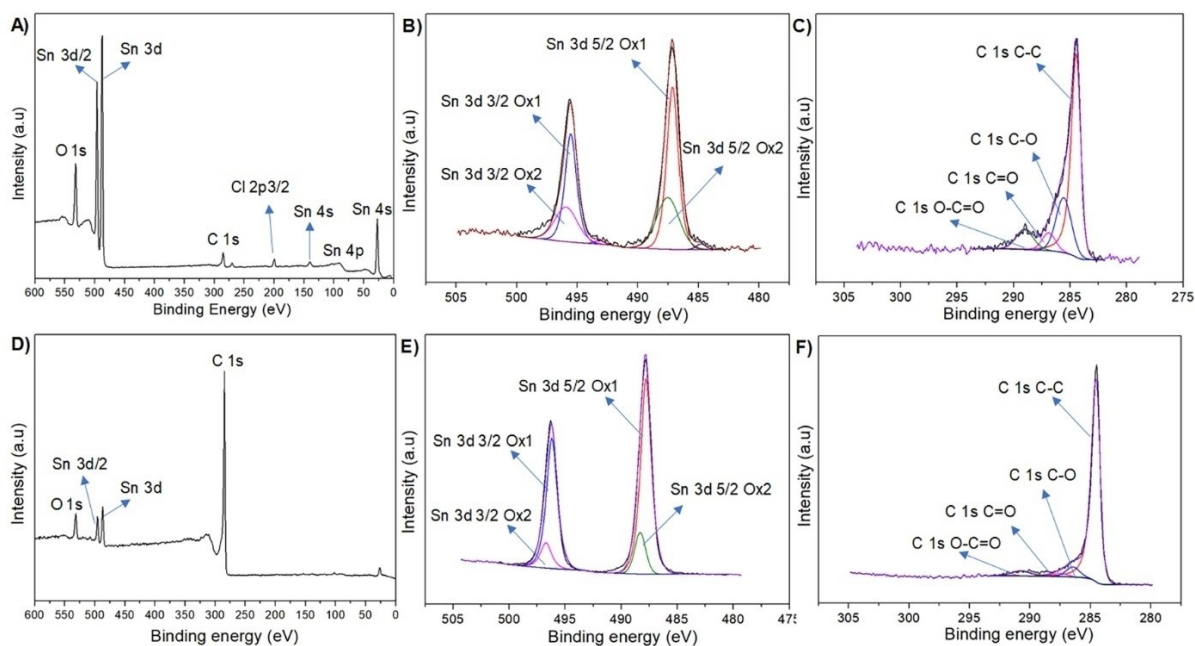

Figure 4. (a) XPS survey analysis of SnO$_2$/CNF. (b) High resolution scan of Sn from SnO$_2$/CNF. (c) High resolution scan of C from SnO$_2$/CNF. (d) XPS survey analysis of Sn/CNF. (e) High resolution scan of Sn from Sn/CNF. (f) High resolution scan of C from Sn/CNF.

in O content between SnO$_2$/CNF and Sn/CNF shows that the heat treatment under Ar atmosphere has reduced the amount of oxygen containing functional groups from the surface of the CNF and formed mostly Sn–C–Sn bonding. The high carbon content in Sn/CNF compared to SnO$_2$/CNF also suggests that the SnO$_2$ is mostly decomposed at high temperature and CNF is

coated with tin (Table S2 supporting information). High resolution scans of the C1s region reveal that this consists mainly of graphitised sp^2 carbon. There is a significant increase in the proportion of C–C component between SnO$_2$/CNF (60.2%) and Sn/CNF (87.9%) which is unsurprising given the large decrease in O content between the samples. Closer comparison and

Batteries & Supercaps

Research Article
doi.org/10.1002/batt.202300474

Chemistry Europe
European Chemical
Societies Publishing

deconvolution of the Sn 3d high resolution scans show the emergence of a small peak at 484.8 eV for Sn/CNF which represents metallic tin, but oxides of tin are still the major component. The high-resolution scans of the oxygen region for both materials are shown in Figure S4 where oxygen contents are significantly reduced with the Sn—O in Sn/CNF.

Redox Chemistry and Electrochemical Performance of Sn/CNF and SnO₂/CNF

The electrochemical cycling tests performed in the presence of SnO_2/CNF and Sn/CNF are shown in Figure 5a&c, respectively, while their respective charge/discharge profiles are shown in Figure 5b&d. An SEM image of the pristine carbon paper as an anode is presented in Figure S2. It can be clearly seen that the SnO_2/CNF displays unstable cycling behaviour over 1400 cycles (Figure 5a) with considerable voltage loss (Figure 5b). Conversely, the Sn/CNF based ZBB demonstrates stability over 3000 cycles with minimal electrochemical disturbance (Figure 5c) and shows a voltage loss of ~500 mV (Figure 5d) compared to the SnO_2/CNF. At a constant current of 10 mA cm^{-2}

and 1.64 mAh capacity/cycle, the total accumulative capacities drawn from both batteries amount to 4800 mAh (Sn/CNF based battery) and 2240 mAh (SnO_2/CNF based battery) over 3000 and 1400 cycles, respectively. Both batteries exhibited similar coulombic efficiencies, at approximately 87% for SnO_2/CNF and 89% for Sn/CNF. However, while the Sn/CNF based ZBBs showed a ~500 mV loss (Figure 5d) the SnO_2/CNF based ZBB exhibited a much higher loss of 736 mV (Figure 5b). This discrepancy underscores the superior electrochemical kinetics of Sn/CNF, owing to its more electrically conductive Sn—C—Sn structure compared to the Sn—O—C in the SnO_2/CNF (Figure 5i). Despite concerns about bromine's corrosive nature to metallic tin, the relatively low mass loading of tin and its physical interaction with the CNF based carbon matrix make the Sn/CNF act as an efficient catalyst for Br-/Br₂ redox reactions. High-resolution TEM images in Figure 3d indicate that there is an amorphous carbon layer enveloping the tin particle, acting as a protective shield against tin reaction with bromine. This assertion is substantiated by the XPS analysis, indicating a substantial carbon peak and tin content in Sn/CNF (Table S1). Additionally, the weight reduction of Sn/CNF by nearly 50% compared to the initial weight of SnO_2/CNF post high temper-
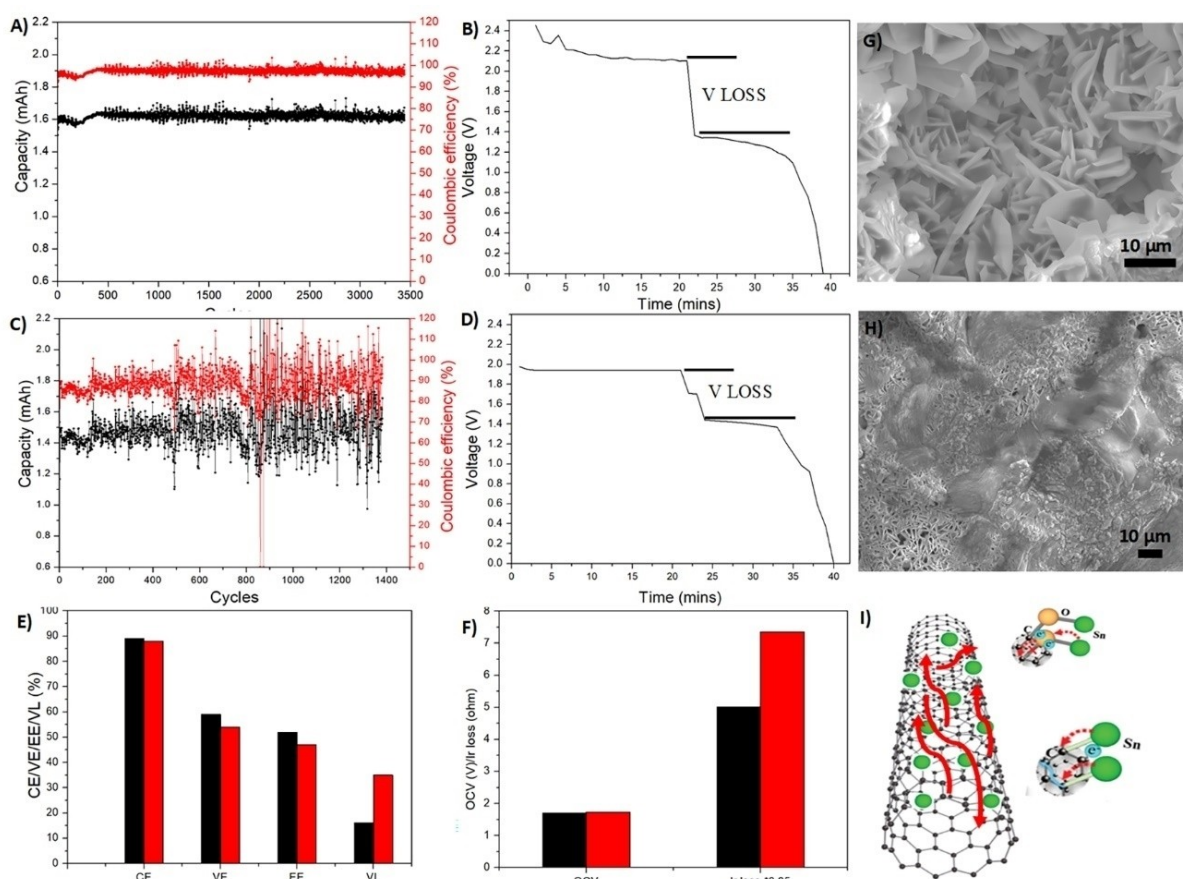

Figure 5. (a) Electrochemical cycling performance of SnO_2/CNF cathode based ZBB. (b) Charge/discharge profile of SnO_2/CNF cathode based ZBB. (c) Electrochemical cycling performance of Sn/CNF cathode based ZBB. (d) Charge/discharge profile of Sn/CNF cathode based ZBB. (e) Coulombic (CE), voltaic (VE) and energy efficiencies (EE) and voltage loss (VL) for both SnO_2/CNF and Sn/CNF (red represents SnO_2/CNF and black represents Sn/CNF). (f) OCV and IR loss for both SnO_2/CNF and Sn/CNF (red represents SnO_2/CNF and black represents Sn/CNF). (g) SEM image of fully charged anode shows Zinc morphology from the SnO_2/CNF based ZBB. (h) SEM image of fully charged anode shows Zinc morphology from the Sn/CNF based ZBB. (i) Electron distribution comparison of SnO_2/CNF and Sn/CNF.

ature treatment and washing, suggests the breakdown of most tin oxide bonds, leaving behind physically interacting tin with the CNF. Consequently, Sn/CNF surpasses the SnO₂/CNF based ZBB in coulombic efficiency (CE), voltaic efficiency (VE) and energy efficiency (EE) (Figure 5e), primarily due to the lower electrical conductivity of the Sn—O—C bonding, insufficient for electron access to the Br⁻ compared to Sn—C—Sn in Sn/CNF (Figure 5i). Post-cycling SEM analysis of the zinc-plated electrode (Figure 5g, h) reveals a rougher and more porous surface in SnO₂/CNF based ZBB, contrasting the uniform and compact surface morphology of the Sn/CNF based ZBB, devoid of dendrite growth or pores.

The stability of the open-circuit voltage (OCV) in the ZBB indicates its electrochemical stability and resistance to self-discharge. During charging, OCV decreases due to bromine migration to the anode and the cycling instability attributed to inadequate zinc plating. While both ZBBs exhibit a similar average OCV, the Sn/CNF based battery outperforms the SnO₂/CNF based ZBB in terms of IR loss. This larger IR loss in SnO₂/CNF based ZBB implies greater polarization and slower electrochemical reactions, suggesting ineffective acceleration of electrochemical reaction compared to the Sn/CNF based ZBB.

Redox Mechanism Analysis by DFT

To confirm the superiority of Sn in improving the performance of ZBBs, the adsorption characteristics of Br atoms on SnO₂ and
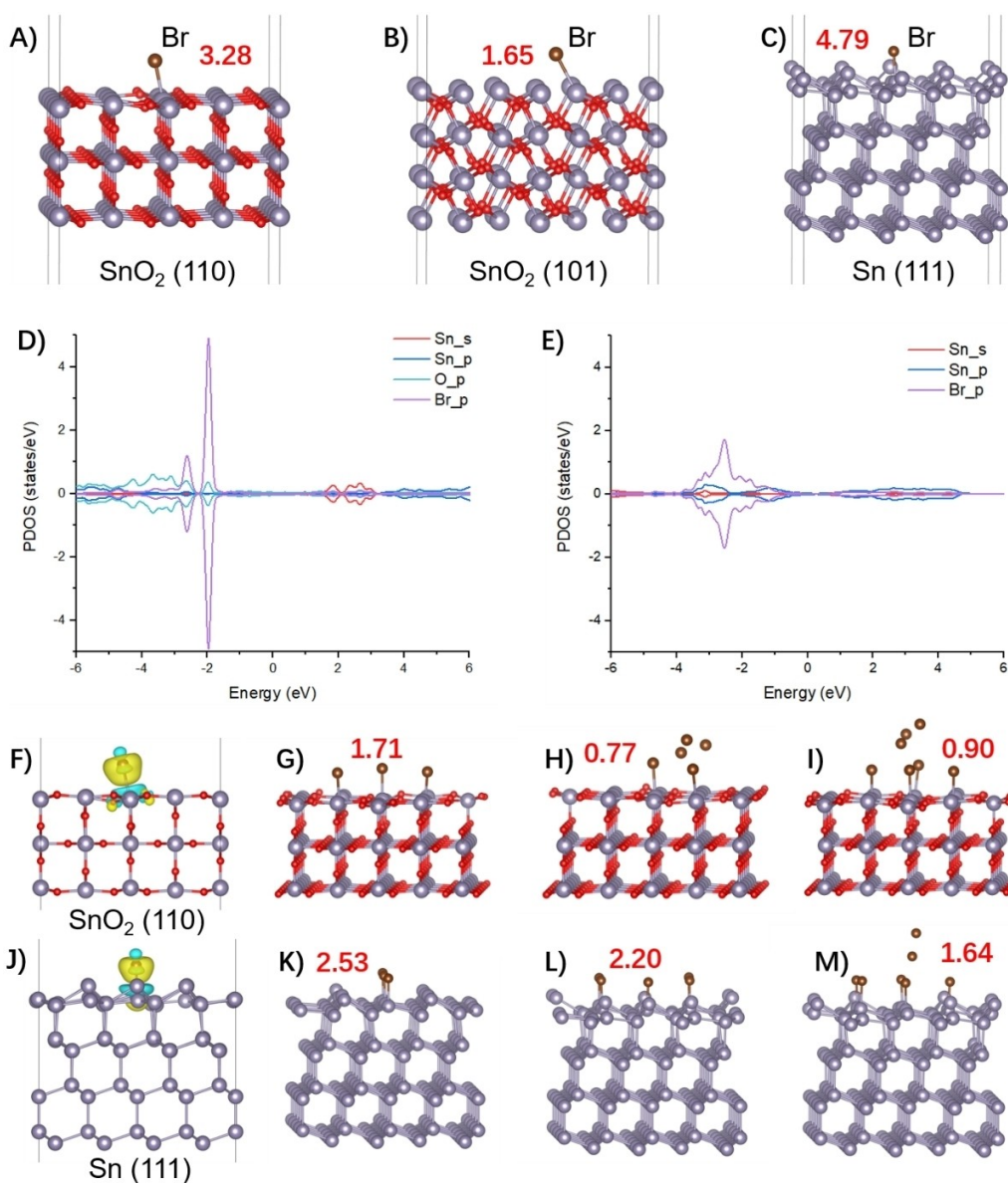

Figure 6. The adsorption structures of Br on (a) SnO₂ (110), (b) SnO₂ (101), and (c) Sn (111) surfaces. (d, e) the SnO₂ (110) and Sn (111) surfaces with respect to the projected density of states (PDOS). The projected DOS and (f, j) the charge density differences of SnO₂ (110) (the iso-value of the surfaces is 0.002 e bohr⁻¹) and Sn (111) surfaces with an adsorbed Br atom. The structures of (g–i) SnO₂ (110) surface and Sn (111) with 3, 5, and 7 Br atoms adsorbed, respectively. The red fonts are the corresponding binding energy of Br per atom in the unit of eV.
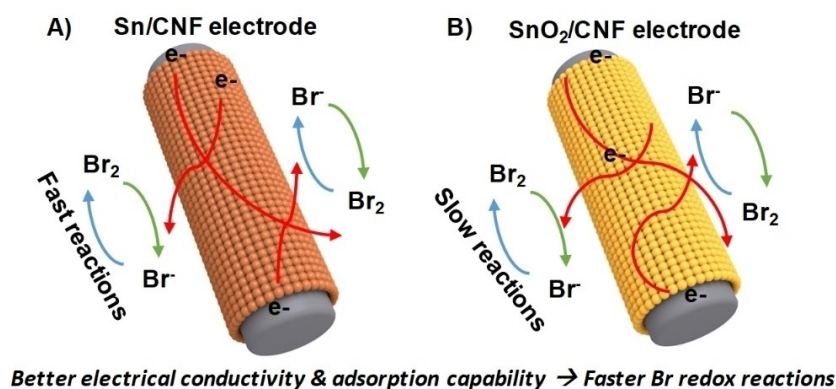
Figure 7. Schematic illustration to represent the Br^-/Br_2 redox reaction in the presence of (a) Sn/CNF and (b) SnO_2/CNF based electrodes.

Sn surfaces were compared. Firstly, the binding energies of a Br atom on SnO_2 (110), (b) SnO_2 (101), and Sn (111) surfaces were compared, as shown in Figure 6(a–c). The Sn (111) surface shows highest binding energy of 4.79 eV to Br, followed by SnO_2 (110) surfaces (3.28 eV). To understand the origin of the high binding energy, the SnO_2 (110) and Sn (111) surfaces were further studied with respect to the projected density of states (PDOS). The PDOS of Br_p orbitals are more localized in the SnO_2…Br system, and the corresponding energy is higher. In addition, the PDOS of Sn_s at the energy of ~2 eV indicates an anti-bonding state that increases the energy of the system. On the other hand, in the Sn…Br system, the PDOS of Br_p is dispersive in lower energy and has a better overlap with the PDOS of Sn_p orbitals, which lowers the energy of the system. The charge density differences of the two systems show that the electrons mainly transfer from the Sn atom on the surface to Br atom, while the surrounding O atoms in the SnO_2…Br system also take electrons from the Sn atom which probably creates the high energy states of Sn_s orbitals. When the density of the Br atoms on the surface is increased, the average binding energies of Br quickly decrease on the SnO_2 (110) surface, while those on Sn (111) surfaces remain at a high level. Especially, when 7 atoms are adsorbed on the Sn (111) surface, the average binding energy of Br is 1.64 eV, which can provide a favourable adsorption thus a better electrochemical performance.

The observed superior performance of Sn/CNF over SnO_2/CNF in this study should be attributed to the strong electronic interaction between Sn particles with the CNF that can provide more nucleation sites and electronic conductivity for faster Br^-/Br_2 redox reaction. The mechanism of the Br^-/Br_2 redox reaction is schematically illustrated in Figure 7. During the charging/discharging process, the Br^-/Br_2 has faster electrochemical kinetics due to higher electronic conductivity of the Sn nanoparticles/CNF with rich Sn–C–Sn bonding (Figure 7a). However, electrons in SnO_2/CNF with more Sn–O–C structure are less available for the Br^-/Br_2 redox reaction (Figure 7b) due to the lower electronic conductivity. Moreover, the strong adsorption capability of metallic tin to Br from DFT calculations as described above could be another reason for the enhanced electrochemical performance of Sn/CNF electrode.

Conclusions

In summary, we have successfully developed tin-modified carbon nanofibers using a straightforward two-step approach and demonstrated its application as an efficient catalytic electrode for Br redox reactions in ZBBs. By fabricating static ZBBs using SnO_2/CNF and Sn/CNF, we explored their electrochemical kinetics. The electron conductive framework of Sn/CNF notably enhances the catalytic activity for the Br_2/Br^- couples. Its Sn–C–Sn structure facilitates faster electron transfer compared to Sn–O–C, resulting in improved electrochemical performance and minimized the voltage loss, thereby enhancing energy efficiency. Moreover, the Sn/CNF contributes to stable OCV, prevents dendrite formation, and promotes smooth zinc plating. The static ZBB employing Sn/CNF as catalytic electrode demonstrated exceptional long-term cycling stability (3000 cycles) with a voltage loss of ~500 mV. In contrast, the SnO_2/CNF-based ZBB exhibited a voltage loss of 736 mV and showed limited and unstable cycling performance (1400 cycles). This approach stands as a highly effective method to enhance the electrochemical kinetics of the zinc bromine-based batteries, showcasing considerable promise for static large-scale energy storage applications.

Experimental Section

Sn/CNF synthesis process: The tin decorated carbon nanofiber (Sn/CNF) was synthesized by a hydrothermal method and subsequent heat treatment process. Briefly, commercial CNF (2 g) with an average diameter of 5–8 μm was dispersed in nitric acid HNO_3 (80 mL) and deionized water (20 mL) by sonication at 25°C for 60 mins. Then the tin precursor, $SnCl_2 \cdot 2H_2O$ (3 g) was added into the above solution with stirring for 2 hours at ambient temperature. The resulting solution was transferred into a 100 mL Teflon-lined stainless-steel autoclave and maintained at 200°C for 3 hours. The CNF was collected and heated at 60°C *in-vacuo* for 8 hours to obtain SnO_2/CNF. Surface treatment of CNFs in HNO_3 produced a large amount of reactive functional groups including –COOH and –OH groups, which act as nucleation sites for SnO_2 nanoparticles.[22] Sn–O–C bonds were formed between SnO_2 and CNF in the SnO_2/CNF. The SnO_2/CNF was further heated at 500°C in the presence of argon to obtain the Sn/CNF. During thermal treatment, most

Sn–O–C bonds were broken down to form Sn–C bonds, which was denoted as Sn–C–Sn.

Characterization techniques: Field emission transmission electron microscopy (FE-TEM F20) was used to investigate the SnO_2 and Sn CNF structures. The morphology and composition of the SnO_2/CNF and Sn/CNF samples were characterized using a scanning electron microscope (SEM) (JEOL-7001F). XPS survey data were acquired using a Kratos Axis Supra Plus X-ray photoelectron spectrometer incorporating a 165 mm hemispherical electron energy analyzer. The incident radiation was monochromatic Al Kα X-rays (1486.6 eV) at 150 W (15 kV, 10 mA). Survey (wide) scans were taken at an analyser pass energy of 160 eV and multiplex (narrow) high resolution scans at 20 eV. Survey scans were carried out over 1200–0 eV binding energy range with 1.0 eV steps and a dwell time of 100 ms. Narrow high-resolution scans were run with 0.05 eV steps and at a dwell time of 250 ms. During analysis the pressure in the analysis chamber was better than 1.0×10^{-8} Torr. Atomic concentrations were calculated using the CasaXPS version 2.3.14 software with Kratos library relative sensitivity factors (RSFs). Peak fitting of the high-resolution data was also carried out using the CasaXPS software. X-ray diffraction (XRD) of SnO_2/CNF and Sn/CNF samples were analyzed on a Bruker D8 Advance Powder X-ray diffractometer equipped with a Cu source, operated at 40 kV and 40 mA, and an energy discriminating 2D array detector that minimizes a fluorescent background. Data were collected using a Bragg–Brentano geometry with a 0.12 deg divergence slit from 5 deg to 80 deg two-theta at a resolution of 0.02 deg and at 1.2 s per step.

Computational Details: The adsorption capability of different substrates to Br were evaluated using Vienna Ab initio Simulation Package (VASP) based on density functional theory (DFT).[23] The surface slabs were created by slicing their corresponding bulks along specified lattice planes. The Perdew-Burke-Ernzerhof functional of generalized gradient approximation was used to describe the exchange–correlation interactions.[24] The energy cut-off for plane waves is 520 eV. The scattering density of the k-mesh is $0.04*2\pi/\text{Å}$. For electronic self-convergence iteration, the energy threshold is set to 10^{-5} eV per cell, and for the ionic relaxation, the convergence criterion is the force of the atoms less than 0.02 eV/Å. For adsorption simulations, the van der Waals force was corrected by Grimme-D3 method.[25]

Electrochemical Measurements: The ZBBs battery performance was tested in a galvanostatic mode using a LAND system within a voltage window of 0–2 V (Zn/Zn^{2+}) at constant current rate. Nafion membrane was used as a separator to conduct the experiments. The electrolyte was an aqueous solution of $ZnBr_2$ (Zinc Bromide-2.5 M), Potassium chloride (KCL-1 M), MEP (1-ethyl-1-methyl Pyrrolidone-1 M), and Zinc Chloride ($ZnCl_2$-0.5 M). Total 500 μL of electrolyte was used in the Swagelok cell.

Supporting Information

Supporting Information is available from the Wiley Online Library or from the author.

Conflict of Interests

The authors declare no conflict of interest.

Data Availability Statement

The data that support the findings of this study are available from the corresponding author upon reasonable request.

[1] Z. Yang, J. Zhang, M. C. Kintner-Meyer, X. Lu, D. Choi, J. P. Lemmon, J. Liu, *Chem. Rev.* **2011**, *111*, 3577.
[2] G. L. Soloveichik, *Chem. Rev.* **2015**, *115*, 11533.
[3] V. Arunachalam, E. Fleischer, *MRS Bull.* **2008**, *33*, 264.
[4] P. J. Meier, P. P. Wilson, G. L. Kulcinski, P. L. Denholm, *Energy Policy* **2005**, *33*, 1099.
[5] M. Jaforullah, A. King, *Energy Economics* **2015**, *49*, 711.
[6] L. Bardwell, L. Blackhall, M. Shaw, *Energy Policy* **2023**, *173*, 113409.
[7] B. Goldstein, T. G. Reames, J. P. Newell, *Energy Research and Social Science* **2022**, *84*, 102365.
[8] S. Biswas, A. Senju, R. Mohr, T. Hodson, N. Karthikeyan, K. W. Knehr, A. G. Hsieh, X. Yang, B. E. Koel, D. A. Steingart, *Energy Environ. Sci.* **2017**, *10*, 114.
[9] C. Xie, Y. Liu, W. Lu, H. Zhang, X. Li, *Energy Environ. Sci.* **2019**, *12*, 1834.
[10] J. H. Lee, Y. Byun, G. H. Jeong, C. Choi, J. Kwen, R. Kim, I. H. Kim, S. O. Kim, H. T. Kim, *Adv. Mater.* **2019**, *31*, 1904524.
[11] L. Gao, Z. Li, Y. Zou, S. Yin, P. Peng, Y. Shao, X. Liang, *iScience* **2020**, *23*, 101348.
[12] C. Wang, W. Lu, Q. Lai, P. Xu, H. Zhang, X. Li, *Adv. Mater.* **2019**, *31*, 1904690.
[13] M. Wu, H. Jiang, R. Zhang, L. Wei, K. Y. Chan, T. Zhao, *Electrochim. Acta* **2019**, *318*, 69.
[14] W. Lu, P. Xu, S. Shao, T. Li, H. Zhang, X. Li, *Adv. Funct. Mater.* **2021**, *31*, 2102913.
[15] C. Wang, Q. Lai, P. Xu, D. Zheng, X. Li, H. Zhang, *Adv. Mater.* **2017**, *29*, 1605815.
[16] Y. Zeng, Z. Yang, F. Lu, Y. Xie, *Appl. Energy* **2019**, *255*, 113756.
[17] K. Amini, J. Gostick, M. D. Pritzker, *Adv. Funct. Mater.* **2020**, *30*, 1910564.
[18] Y. Cheng, J. Huang, H. Qi, L. Cao, J. Yang, Q. Xi, X. Luo, K. Yanagisawa, J. Li, *Small* **2017**, *13*, 1700656.
[19] H. Luo, G. Xiong, Z. Yang, Q. Li, C. Ma, D. Li, X. Wu, Z. Wang, Y. Wan, *Mater. Res. Bull.* **2014**, *53*, 123.
[20] C. Wronski, *Br. J. Appl. Phys.* **1967**, *18*, 1731.
[21] H. Jiang, K.-s. Moon, H. Dong, F. Hua, C. Wong, *Chem. Phys. Lett.* **2006**, *429*, 492.
[22] C. Santato, C. M. López, K.-S. Choi, *Electrochem. Commun.* **2007**, *9*, 1519.
[23] G. Kresse, J. Furthmüller, *Phys. Rev. B* **1996**, *54*, 11169.
[24] J. P. Perdew, K. Burke, M. Ernzerhof, *Phys. Rev. Lett.* **1996**, *77*, 3865.
[25] S. Grimme, J. Antony, S. Ehrlich, H. Krieg, *J. Chem. Phys.* **2010**, *132*, 154104.